Bifurcation analysis of multiple steady flow patterns for Rayleigh-Bénard convection in a cubical cavity at Pr=130

D. Puigjaner
Departament Enginyeria Informatica i Matematiques, Universitat Rovira i Virgili, Tarragona, Catalunya, Spain

J. Herrero and Francesc Giralt*
Departament Enginyeria Quimica, Universitat Rovira i Virgili, Tarragona, Catalunya, Spain

C. Simó
Departament Matematica Aplicada i Analisi, Universitat de Barcelona, Barcelona, Catalunya, Spain
(Received 3 January 2006; published 7 April 2006)

The bifurcation diagram of steady convective flow patterns inside a cubical cavity with adiabatic lateral walls heated from below and filled with silicone oil (Pr=130) was determined for values of the Rayleigh number (Ra) up to 1.5×10^5. A continuation procedure based on the Galerkin spectral method was used to determine the steady convective solutions as a function of Ra. Bifurcations leading to either new steady or time-dependent solutions were identified and new steady solution branches were also continued. A total of fifteen steady solutions were tracked and the stability analysis predicted that six flow patterns were stable and that two, three, or even four of these patterns coexisted over certain ranges of Ra in the studied domain. Predicted flow patterns and transitions are in agreement with flow visualizations previously reported in the literature. The variation of the Nusselt number (Nu) as a function of Pr was investigated for three of the stable flow patterns identified: a *x* or *y* roll, a diagonal oriented roll and a pattern formed by four connected half rolls. It was found that whereas the Nusselt changes within the region $0.71\leqslant \mathrm{Pr}\leqslant 10$ it tends to an asymptotic value with increasing Pr.

DOI: 10.1103/PhysRevE.73.046304 PACS number(s): 44.25.+f, 47.20.Bp, 47.10.Fg, 47.11.Kb

I. INTRODUCTION

Rayleigh-Bénard convection in parallelepipedical and cylindrical enclosures has been widely studied [1–3] because it has many applications and it is the simplest multiple-scale coupled nonlinear fluid flow problem where hydrodynamic instabilities [4–9] and the onset and development of turbulence can be investigated [10–17]. Convection starts when the Rayleigh number reaches a critical value Ra_c. The drag exerted by lateral walls in confined domains increases the value $\mathrm{Ra}_c=1708$ obtained for infinite parallel plates [4]. Several numerical linear stability analysis [5,6,8,9,18] report on the variation of Ra_c with respect to the width/height and length/height aspect ratios for parallelepipedical cavities. These studies also identify the flow pattern represented by the eigenvector associated to the zero eigenvalue at the onset of convection; the flow pattern at Ra slightly above the critical value is very similar to the eigenvector associated with the zero eigenvalue.

Studies based on linear stability analysis cannot determine which kind of flow will occur when Ra_c is associated to a multiple eigenvalue, as it occurs in a cubical cavity. In this case a bifurcation analysis is needed to determine which combinations of the independent eigenvectors take place. In addition, numerical bifurcation and parameter continuation methods applied to the nonlinear governing equations are also needed to calculate the bifurcation diagram of the flow. Numerical and experimental studies [9,19,20] conclude that the intrinsic symmetries of the cubical geometry yield steady state solutions with manifold symmetries different from those in rectangular enclosures. Hence, symmetry-breaking bifurcations are likely to take place in the case of the cubical geometry and, consequently, rather complex bifurcation diagrams can be expected.

The bifurcation diagram of steady convective flow patterns in a cubical cavity with adiabatic lateral walls and filled with air (Pr=0.71) was recently reported by Puigjaner *et al.* [19]. In this work the five steady flow patterns indicated in Fig. 1(b) were identified to be stable over some ranges of the Rayleigh number for $\mathrm{Ra}<1.5\times10^5$. On the other hand, Pallarès *et al.* [20] experimentally observed three different steady flow patterns in a cubical cavity with adiabatic lateral walls filled with silicone oil (Pr=130). The experiments were performed in the range $\mathrm{Ra}<8\times10^4$ and several transitions between the identified flow patterns were observed as Ra was continuously varied from the conductive state.

The aim of the present work is to determine the bifurcation diagram of steady convective flow patterns that develop inside a cubical cavity with adiabatic lateral walls filled with silicone oil (Pr=130) for $\mathrm{Ra}\leqslant1.5\times10^5$. Stable and unstable steady solution branches are tracked using a parameter continuation procedure based on a Galerkin method and both steady and Hopf bifurcation points are identified. Unstable flow patterns are also considered because they can become stable as a consequence of subsequent bifurcations. The evolution of the spatial configuration of stable flow patterns and their heat transport properties is studied as the Ra increases. Predicted flow patterns and transitions are compared with previously reported experimental results [20]. In addition,

*Electronic address: fgiralt@urv.cat

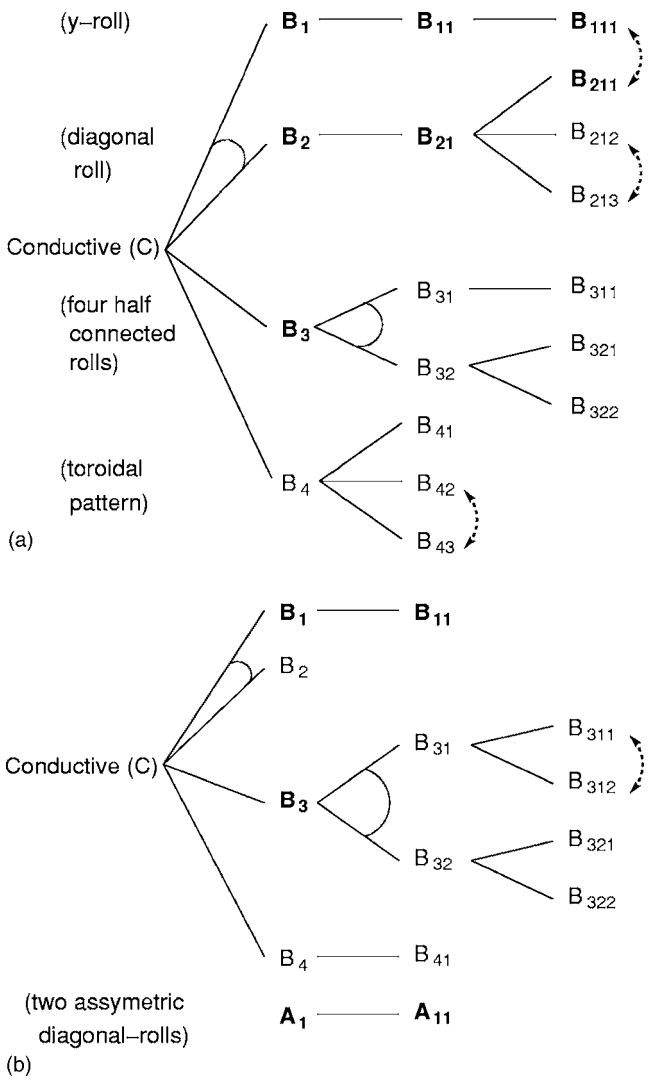

FIG. 1. Sketches of the bifurcation diagrams at (a) Pr=130 and (b) Pr=0.71. Solutions that are connected by a dashed arrow represent the same flow pattern. Solutions that set in at the same bifurcation point are joined with a solid arc. Those flow patterns printed in boldface are stable over certain ranges of Rayleigh numbers for $\mathrm{Ra} \leqslant 1.5 \times 10^5$.

the effect of the Prandtl number on the heat transfer properties is analyzed for three stable flow patterns.

II. MATHEMATICAL FORMULATION AND NUMERICAL METHOD

A. Governing equations

The nondimensional domain scaled by the length of the side of the cubical cavity, L, is given by $\Omega = [-\frac{1}{2}, \frac{1}{2}] \times [-\frac{1}{2}, \frac{1}{2}] \times [-\frac{1}{2}, \frac{1}{2}]$. An incompressible flow of a Newtonian fluid is assumed and the Boussinesq model is used, i.e., all of the fluid properties are assumed to be constant except for a linear variation of density (ρ) with temperature in the buoyancy term of the Navier-Stokes equations. The governing dimensionless nonlinear equations for the velocity $\mathbf{V} = (u, v, w)$, the temperature departure from the motionless conductive state, θ, and the pressure, p, are

$$\frac{1}{\mathrm{Pr}}\left(\frac{\partial \mathbf{V}}{\partial t} + \mathrm{Ra}^{1/2}(\mathbf{V}\cdot\nabla)\mathbf{V}\right) - \nabla^2\mathbf{V} - \mathrm{Ra}^{1/2}\theta\mathbf{e_z} + \nabla p = \mathbf{0}, \tag{1}$$

$$\frac{\partial \theta}{\partial t} + \mathrm{Ra}^{1/2}(\mathbf{V}\cdot\nabla)\theta - \nabla^2\theta - \mathrm{Ra}^{1/2} w = 0, \tag{2}$$

$$\nabla\mathbf{V} = 0. \tag{3}$$

In Eq. (1) $\mathbf{e_z}$ denotes the unit vector in the z direction. Velocity, temperature, time, and pressure are scaled according to $q_0 = [\beta(\Delta\theta) g L \alpha/\nu]^{1/2}$, $\Delta\theta$, L^2/α, and $\rho\nu q_0/L$, respectively, where g is the acceleration of gravity, β is the coefficient of thermal expansion, ν is the kinematic viscosity, α is the thermal diffusivity, T_c and T_h are the temperatures at the top and the bottom horizontal walls, respectively and $\Delta\theta = T_h - T_c$. The Rayleigh number and the Prandtl number are defined as $\mathrm{Ra} = \beta(\Delta\theta) g L^3/\alpha\nu$ and $\mathrm{Pr} = \nu/\alpha$, respectively. By assuming six rigid walls and four adiabatically insulated lateral walls the boundary conditions may be written as

$$\mathbf{V} = \theta = \mathbf{0} \quad \text{at } |z| = \tfrac{1}{2}, \tag{4}$$

$$\mathbf{V} = \frac{\partial\theta}{\partial x} = \mathbf{0} \quad \text{at } |x| = \frac{1}{2}, \tag{5}$$

$$\mathbf{V} = \frac{\partial\theta}{\partial y} = \mathbf{0} \quad \text{at } |y| = \frac{1}{2}. \tag{6}$$

Equations (1)–(6) do not change when x and u are respectively replaced by $-x$ and $-u$ or when y and v are respectively replaced by $-y$ and $-v$. Hence, any flow pattern is equally realizable in four particular solutions depending on the sign of the x and y vorticity components. In addition, due to the symmetry of the cubical geometry any particular solution of Eqs. (1)–(6) yields another solution that is obtained by exchanging (x, y, z) and (u, v, w) for (y, x, z) and (v, u, w), respectively. Thus, once a particular solution of Eqs. (1)–(6) has been found seven more solutions can be generated by using the symmetry properties of equations and geometry. Two or more of these eight particular solutions may coincide provided that they verify some symmetry properties.

B. Numerical method

1. Continuation procedure

The continuation procedure reported by Puigjaner *et al.* [19] was applied to determine the bifurcations and stability of the steady solutions of Eqs. (1)–(3), subject to boundary conditions (4)–(6), as a function of Ra. The numerical procedure, which is summarized in this section, was based on a Galerkin spectral method with a complete set of basis functions satisfying all boundary conditions. A formulation of the velocity in terms of scalar potential functions ensured that continuity equation was automatically fulfilled and that pressure was not present in the final equations.

The velocity and temperature fields were approximated by the truncated expansion

$$\begin{pmatrix} \mathbf{V} \\ \theta \end{pmatrix} = \sum_{i=1}^{N_x} \sum_{j=1}^{N_y} \sum_{k=1}^{N_z} \sum_{s=1}^{4} a_{ijk}^{(s)} \mathbf{G}_{ijk}^{(s)}, \tag{7}$$

where $a_{ijk}^{(s)}$ are the unknown time-dependent coefficients, and $\mathbf{G}_{ijk}^{(s)}$ are the elements of a complete set of divergence-free basis functions which are defined as products of trigonometric functions and the so-called beam-functions documented by Harris and Reid [21]. The three subscripts and the four superscripts in expressions (7) can be collapsed into a single one for the sake of clarity

$$\begin{pmatrix} \mathbf{V} \\ \theta \end{pmatrix} = \sum_{l=1}^{N} c_l \mathbf{F}_l. \tag{8}$$

In expression (8) coefficients c_l are the unknowns, $\mathbf{F}_l$ represents a function $\mathbf{G}_{ijk}^{(s)}$ for some values of i, j, k, and s, and $N=32\times N_x\times N_y\times N_z$.

Application of the Galerkin method with expansion (8) reduces the nonlinear problem (1)–(3) to the following system of ordinary differential equations (ODE's):

$$\sum_i \left(B_{ji}(\mathrm{Pr}) \frac{dc_i(t)}{dt} \right) = f_j(\mathrm{Pr},\mathrm{Ra},t,\mathbf{c}), \quad j=1,\ldots,N, \tag{9}$$

with

$$f_j(\mathrm{Pr},\mathrm{Ra},t,\mathbf{c}) := \sum_i [L_{ji}(\mathrm{Ra})c_i(t)] - \mathrm{Ra}^{1/2} \sum_{i,n} [Q_{jin}(\mathrm{Pr})c_i(t)c_n(t)], \quad j=1,\ldots,N. \tag{10}$$

The matrices with components L_{ji} and Q_{jin} given by Eq. (10) contain the coefficients of the linear and nonlinear terms of Eq. (9), respectively [19]. The matrix B_{ji}, which multiplies the time derivative terms, is called mass matrix. For steady solutions the left hand side of Eq. (9) is zero and the problem reduces to the set of algebraic equations

$$\sum_i [L_{ji}(\mathrm{Ra})c_i] - \mathrm{Ra}^{1/2} \sum_{i,n} [Q_{jin}(\mathrm{Pr})c_i c_n] = 0, \quad j=1,\ldots,N. \tag{11}$$

In the present work the Prandtl number is fixed (Pr=130) and the Rayleigh number is taken as abscissa in the bifurcation diagram. Thus, Ra is called the bifurcation parameter because the change of behavior of flow patterns is studied as a function of this parameter. Provided that at least one solution $(\mathrm{Ra}_1,\mathbf{c}_1)$ of Eq. (11) has been determined, a predictor-corrector parameter continuation method can be used to calculate further solutions on the branch

$$(\mathrm{Ra}_2,\mathbf{c}_2), \quad (\mathrm{Ra}_3,\mathbf{c}_3), \ldots,$$

until either $\mathrm{Ra}=1.5\times 10^5$ is reached or the branch connects with another tracked solution branch. The eigenvalue problem associated with the asymptotic stability of steady solutions along the different solution branches in the bifurcation diagram was solved by means of the Arnoldi method [22]. Hence, the current analysis extends beyond the region around the critical Rayleigh. Unstable convective flow patterns must also be continued because they can become stable as a consequence of subsequent bifurcations. However, since the number of steady bifurcations was too great, the following criterion was used to select which of the solutions branches emanating at bifurcation points had to be followed. Those convective flow patterns that set in at bifurcations from the motionless conductive solution and that had at most three unstable eigenvalues near the bifurcation point were tracked using the continuation method; secondary bifurcations were identified and steady flow patterns that emanated at those bifurcations and had at most two unstable eigenvalues near the bifurcation point were also continued. Further details of the numerical procedure are described in Refs. [19,23].

TABLE I. Convergence of the Rayleigh number at which bifurcations from different convective flow patterns occur as a function of the truncation parameters $N_t=N_x=N_y=N_z$. The last column includes the relative differences between $N_t=7$ and $N_t=8$.

Flow transitions	$N_t=5$	$N_t=6$	$N_t=7$	$N_t=8$	Δ_{7-8} (%)
$B_1\rightarrow B_{11}$	51601	51290	51145	51074	0.14
$B_{11}\rightarrow B_{111}$	62204	61685	61383	61238	0.24
$B_2\rightarrow B_{21}$	75626	76132	75636	75557	0.10

2. Accuracy assessment

Table I presents the calculated values of the Rayleigh number at which bifurcations from three different convective flow structures discussed in the next section occur. Convergence is satisfactory for the three bifurcations chosen to test accuracy since differences between predictions for $N_t=N_x=N_y=N_z=5$ and $N_t=8$ are always smaller than 1.6%. The results included in Table I also indicate that an increase from $N_t=7$ to $N_t=8$ causes at most a 0.24% change in the bifurcation value Ra_b. One can even extrapolate the data in Table I to $N_t=\infty$ by using a law of the form $a+b/N_t$. The extrapolated values for the three flow transitions $B_1\rightarrow B_{11}$, $B_{11}\rightarrow B_{111}$, and $B_2\rightarrow B_{21}$ are $\mathrm{Ra}_b=50412$, 59868, and 73722, respectively. The differences between the $N_t=7$ data and the extrapolated values are below 2.5% in all cases.

As was previously done in Puigjaner *et al.* [19], results obtained with the Galerkin method are compared with numerical solutions obtained using a fourth order accurate finite-difference solver. Since the computational time needed to carry out the forward integration of the nonstationary equations grows as the Pr increases, the time-marching finite-difference procedure [24] used in Puigjaner *et al.* [19] was adapted to solve the steady equations of motion. Thus, provided that initial approximate solutions are known, the finite-difference solver can calculate both stable and unstable steady solutions at any Prandtl number. The finite difference calculations were performed at some discrete values of the Rayleigh number. Each particular calculation was initialized

TABLE II. Nusselt numbers calculated by the Galerkin continuation method and the relative differences with respect the Nusselt number obtained by the finite-difference solver [24].

Flow pattern	10^{-3} Ra	Nu	Δ (%)	10^{-3} Ra	Nu	Δ (%)
B_1	50	3.099	0.1	150	4.135	0.8
B_2	50	3.257	0.2	150	4.345	1.0
B_3	50	3.518	0.1	150	5.063	1.3
B_4	50	3.458	1.1	150	5.220	2.3
B_{11}	100	4.303	1.2	150	4.828	1.8
B_{21}	80	3.672	0.4	150	4.967	1.5
B_{31}	10	1.693	0.1	150	4.260	1.1
B_{32}	10	1.693	0.1	150	4.646	0.9
B_{41}	12	1.578	0.1	150	4.629	1.9
B_{42}	36	3.027	0.5	106	4.642	2.0
B_{111}	62	3.531	0.5	138	4.109	2.1
B_{212}	120	4.410	1.3			
B_{311}	23	2.327	0.1	150	4.099	1.3
B_{321}	18	2.193	0.1	150	4.494	0.3
B_{322}	100	4.058	0.6	150	4.550	1.0

from the velocity and temperature fields given by the Galerkin-based continuation method. Table II shows that the maximum difference in Nusselt number between Galerkin and finite difference solutions is 2.3% at the highest Rayleigh number studied, i.e., $\mathrm{Ra}=1.5\times10^5$.

III. RESULTS AND DISCUSSION

A. Bifurcation diagram

1. Solutions and symmetries

Bifurcation diagrams turn out to be a very useful graphical tool to show the domains of existence, stability character, and bifurcations of the multiple solutions that may coexist as a function of a parameter. To facilitate the comparison of the current bifurcation diagram with that reported at Pr=0.71 [19], both are summarized in Fig. 1. The motionless conductive state is denoted by C, bifurcations from the conductive state are referred to as *primary bifurcations* and the term *secondary bifurcations* refers to bifurcations from convective flow solutions. Convective flow patterns that set in at a primary bifurcation are labeled B_i and flow patterns developed at bifurcation values of B_i are denoted B_{ij}. Thus, any bifurcation adds a new subscript to the parent name. The value of the more external subscript identifies the order of appearance of the corresponding bifurcation along the parent branch. Note that two different names are assigned to those flow patterns that connect two different bifurcation branches or two different bifurcation values of the same branch. In these cases both possible names are joined by dashed arrows in Fig. 1. The names of the flow patterns that are stable over certain ranges of Ra in the region $\mathrm{Ra}\leqslant1.5\times10^5$ are printed in boldface. A brief description of the spatial configuration of each parent flow pattern is also included in this figure.

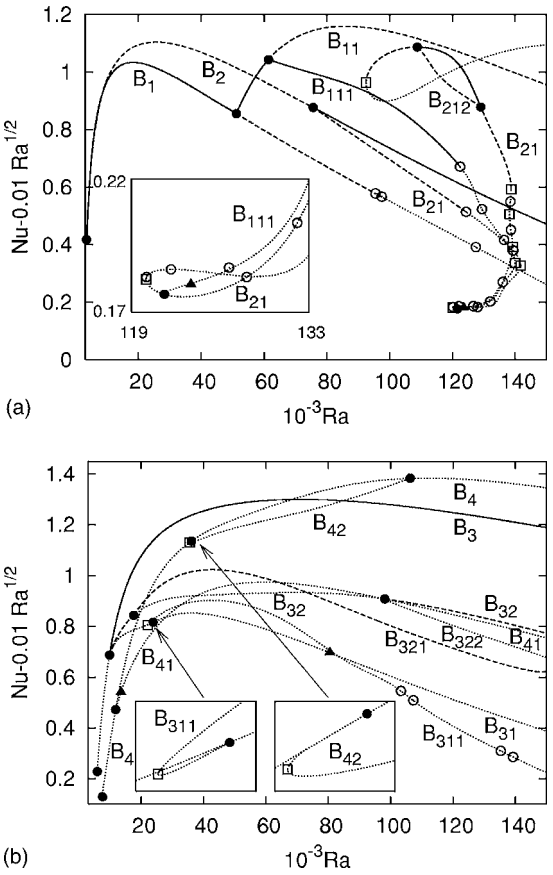

FIG. 2. (a) and (b) Bifurcation diagram at Pr=130. For the sake of clarity the bifurcation diagram is presented in two plots. Stable flow patterns are depicted with solid lines. Unstable flow patterns are represented by dashed lines when they have exactly one unstable eigenmode and by dotted lines when they have two or more unstable eigenmodes. Steady bifurcations are represented by filled circles when the resulting flow patterns have been tracked. Otherwise, steady bifurcations are represented by filled triangles. Hopf bifurcations and turning points are marked with hollow circles and hollow squares, respectively. Additional zooms of smaller domains are included.

The detailed bifurcation diagram for a cubical cavity with adiabatic lateral walls filled with silicone oil (Pr=130) is presented in Fig. 2. This figure depicts the branches of steady solutions in the $(10^{-3}\mathrm{Ra},\mathrm{Nu}-0.01\mathrm{Ra}^{1/2})$ space. The variable $\mathrm{Nu}-0.01\mathrm{Ra}^{1/2}$ is used as ordinate instead of the Nusselt number Nu for the sake of clarity. The Nusselt number Nu is the dimensionless convective heat transport coefficient and was calculated as

$$\mathrm{Nu}=1-\int_{-0.5}^{0.5}\int_{-0.5}^{0.5}\frac{\partial\theta}{\partial z}(x,y,-0.5)dxdy. \qquad (12)$$

Stable flow patterns are depicted with solid lines in Fig. 2. Unstable flow patterns are represented by dashed lines when they have exactly one unstable eigenmode and by dotted lines when they have two or more unstable eigenmodes. Steady bifurcations are represented by filled circles when the resulting flow patterns have been tracked. Otherwise, steady

TABLE III. Summary of the range of existence, the stability character and the symmetry properties of all solutions identified in the bifurcation diagram depicted in Fig. 2. S_x, S_y, S_{d_+}, S_{d_-}, $-Id$, and $-S_y$ are matrix representations of elements of the groups of symmetries and are defined in expressions (13) and (14). The six flow patterns printed in boldface are stable over certain ranges of Rayleigh number for $\mathrm{Ra} \leqslant 1.5 \times 10^5$.

Name	Range of existence	Range of stability	Generators of the symmetry group
$\mathbf{B}_1$	3389–	3389–51155	S_y, $-S_y$
$\mathbf{B}_{11}$	51155–	51155–61383	S_y
$\mathbf{B}_{111}$	61383–140028	61383–122500	
$\mathbf{B}_2$	3389–	75636–	S_{d_-}, $-Id$
$\mathbf{B}_{21}$	75636–	108767–129098	$-Id$
B_{212}	108767–129098		
$\mathbf{B}_3$	5904–	9857–	$-S_y$, S_{d_+}, S_{d_-}
B_{31}	9857–		S_{d_-}
B_{311}	23844–		
B_{32}	9857–		$-S_y$
B_{321}	17613–		
B_{322}	98142–		
B_4	7458–		S_x, S_y, S_{d_+}, S_{d_-}
B_{41}	11781–		S_{d_+}, S_{d_-}
B_{42}	36113–106314		S_x, S_y

bifurcations are represented by filled triangles. Hopf bifurcations and turning points are marked with hollow circles and hollow squares, respectively.

The ranges of Ra where solutions exist and the ranges of Ra where they are stable are summarized in Table III. Since the symmetry properties of a flow pattern are useful to understand its spatial configuration, bases of the groups of symmetries of each steady flow pattern have been identified and included in Table III. Due to the symmetry properties of the governing equations and of the geometry, any flow pattern can be realized in eight different particular solutions (see Sec. III A for details). However, only one particular solution of each flow pattern is discussed in the present work. Thus, the symmetry groups for the flow patterns listed in Table III correspond to just one particular solution.

The elements of the groups of symmetries in Table III are rotations around an axis, reflections with respect to a plane or combinations of both; they can be represented with a 3×3 matrix. Thus, if S belongs to the symmetry group of a flow pattern denoted as B then the transformations $S\mathbf{X}$ and $S\mathbf{V}$, with $\mathbf{X}=(x,y,z)$, $\mathbf{V}=(u,v,w)$, and S a 3×3 matrix, do not change the flow pattern B. In the present work S_x, S_y, S_{d_+}, and S_{d_-} denote reflections with respect to the $x=0$, $y=0$, $x=y$, and $x=-y$ planes, respectively. Their matrix representations are

$$S_x = \begin{pmatrix} -1 & 0 & 0 \\ 0 & 1 & 0 \\ 0 & 0 & 1 \end{pmatrix}, \quad S_y = \begin{pmatrix} 1 & 0 & 0 \\ 0 & -1 & 0 \\ 0 & 0 & 1 \end{pmatrix},$$

$$S_{d_-} = \begin{pmatrix} 0 & -1 & 0 \\ -1 & 0 & 0 \\ 0 & 0 & 1 \end{pmatrix}, \quad S_{d_+} = \begin{pmatrix} 0 & 1 & 0 \\ 1 & 0 & 0 \\ 0 & 0 & 1 \end{pmatrix}. \tag{13}$$

The symmetry with respect to the origin and a rotation of angle π around the y axis are respectively denoted as $-Id$ and $-S_y=-IdS_y$. They are represented by the matrices

$$-Id = \begin{pmatrix} -1 & 0 & 0 \\ 0 & -1 & 0 \\ 0 & 0 & -1 \end{pmatrix} \quad \text{and} \quad -S_y = \begin{pmatrix} -1 & 0 & 0 \\ 0 & 1 & 0 \\ 0 & 0 & -1 \end{pmatrix}. \tag{14}$$

The comparison of the present bifurcation diagram with that reported by Puigjaner *et al.* [19] for $\mathrm{Pr}=0.71$ focuses mainly on those solution branches which are stable over certain ranges of Rayleigh number for $\mathrm{Ra} \leqslant 1.5 \times 10^5$. The only flow patterns connected with the conductive solution that are stable over certain ranges of Ra at $\mathrm{Pr}=0.71$, are those previously denoted as $S1$, $S5$, and $S7$ [19] which correspond to the current B_1, B_3, and B_{11} solutions, respectively. The bifurcation diagram and the variation of the real part of the leading eigenvalues respectively depicted in Figs. 2 and 3 show that for $\mathrm{Pr}=130$ in addition to the B_1, B_3, and B_{11} solutions, three more flow patterns labeled as B_2, B_{21}, and B_{111} are also stable over certain ranges of Ra. Two other stable solutions labeled as A_1 and A_{11} in Fig. 1(b), previously reported as $S8$ and $S10$ flow patterns [19], were identified at $\mathrm{Pr}=0.71$. To investigate the existence of the A_1 isolated branch at $\mathrm{Pr}=130$ a continuation procedure that takes Pr as a parameter was applied at a fixed $\mathrm{Ra}=1.5 \times 10^5$. It should be noted that since the A_1 so-

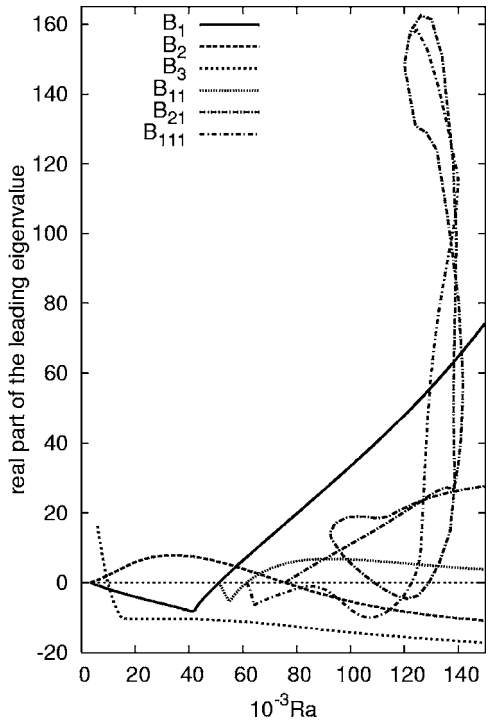

FIG. 3. Variation of the real part of the leading eigenvalue with Ra for those flow patterns that are stable over certain ranges of Ra.

lution branch at Pr=0.71 presents a turning point at Ra =76 800, two different realizations of this flow pattern exist over the range $76\,800 \leqslant \mathrm{Ra} \leqslant 1.5\times10^5$. The evolution of the Nusselt number as a function of the Pr is depicted in Fig. 4 for the two realizations of the A_1 solution at $\mathrm{Ra}=1.5\times10^5$. This figure shows that at Pr=2.476 the two flow patterns have the same Nu. Indeed, the two flow patterns coincide at this point, implying that at Pr=2.476 the turning point of the A_1 solution occurs at $\mathrm{Ra}=1.5\times10^5$. This result suggests that for $\mathrm{Pr}>2.476$ the A_1 isolated branch is shifted to the region $\mathrm{Ra}>1.5\times10^5$, explaining why the A_1 solution was not identified at Pr=130.

2. Primary bifurcations and flow patterns

Linearization of Eq. (11) around the motionless conductive solution shows that primary bifurcations are independent

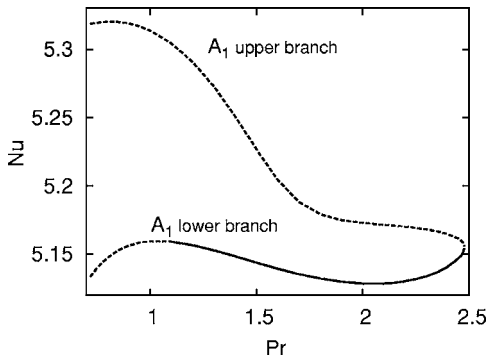

FIG. 4. Variation of the Nusselt number as a function of the Prandtl number for the two branches of the A_1 flow pattern at Ra $=1.5\times10^5$. Stable and unstable flow patterns are plotted with solid and dashed lines, respectively.

of the Prandtl number. Hence, the current predicted values of Ra where the first three primary bifurcations occur, namely $\mathrm{Ra}_c=3389$, $\mathrm{Ra}_b=5902$, and $\mathrm{Ra}_b=7458$, coincide with those previously reported at Pr=0.71 [19]. These values are in good agreement with the values $\mathrm{Ra}_c=3388.5$, $\mathrm{Ra}_b=5901$, and $\mathrm{Ra}_b=7456$ reported by Mizushima and Nakamura [9]. Moreover, the critical Rayleigh number $\mathrm{Ra}_c=3446$ reported by Catton [6] does not differ by more than 2% from the present value. These previous studies [6,9] predicted that the eigenvector associated to the critical value was of the x or y roll type. However, they did not take into account that the critical value corresponds to a double eigenvalue and that, consequently, any linear combination of the two independent eigenvectors, i.e., of one x roll and one y roll, is also an eigenvector of the linear stability problem. When all possible combinations were considered as starting point to calculate possible emanating branches of solutions at this critical value, only an initially stable solution, a x or y roll denoted as B_1 and an initially unstable solution, a diagonal roll denoted as B_2, were identified in the present work. It is worth noting that present results predict that the initially unstable B_2 solution becomes stable at Ra=75 636. Figures 5(a) and 5(b) show that the B_1 solution is a single y roll. The B_2 solution is also a single roll, but with its axis of rotation aligned in the negative diagonal direction, as depicted in Figs. 5(c) and 5(d). It is worth mentioning that in the context of Table III a rotation of π around $x=-y$ can be expressed as $-S_{d\_}=-IdS_{d\_}$. The x roll and the roll aligned in the positive diagonal direction, are obviously equally realizable because of the symmetries of the cubical geometry (see Sec. III A for a detailed discussion of the possible realizations of a flow pattern).

Flow patterns that set in at primary bifurcations are, at values of Ra close to the bifurcation point, very similar to the eigenvector associated with the zero eigenvalue of the linearized equations. Thus, since primary bifurcations are independent of Pr, current solutions B_1, B_2, B_3, and B_4, which set in at primary bifurcations, correspond to flow structures $S1$, $S2$, $S5$, and $S4$ previously reported at Pr=0.71 [19]. The B_1 flow pattern originates in the shape of one y roll. Vertical velocity contours at the horizontal midplane $z=0$ for this flow pattern at Ra=3400 are depicted in Fig. 5(a). This y roll configuration is better portrayed following the method reported by Jeong and Hussain [25]. These authors proposed an identification of a vortex in terms of isosurfaces of the second largest eigenvalue of the symmetric tensor $S^2+\Omega^2$, being S and Ω the symmetric and antisymmetric parts, respectively, of the velocity gradient tensor. Hereinafter, this eigenvalue will be referred to as λ_2 and surfaces of $\lambda_2=0$ will be depicted. Figure 5(b) shows that the y roll configuration of B_1 is well characterized when the surface of $\lambda_2=0$ is depicted. The B_2 flow pattern has also a roll configuration when it develops, but in this case the roll is aligned along the diagonal, as shown in Figs. 5(c) and 5(d). Figures 6(a) and 6(b) shows that at values of Ra slightly above the bifurcation point, the B_3 flow pattern can be understood as four half rolls which are connected between themselves. The toroidal configuration of the B_4 solution is shown in Figs. 6(c) and 6(d).

Figure 7 shows that at $\mathrm{Ra}=1.5\times10^5$ the spatial configurations of the B_1 (unstable), B_2 (stable), B_3 (stable), and B_4

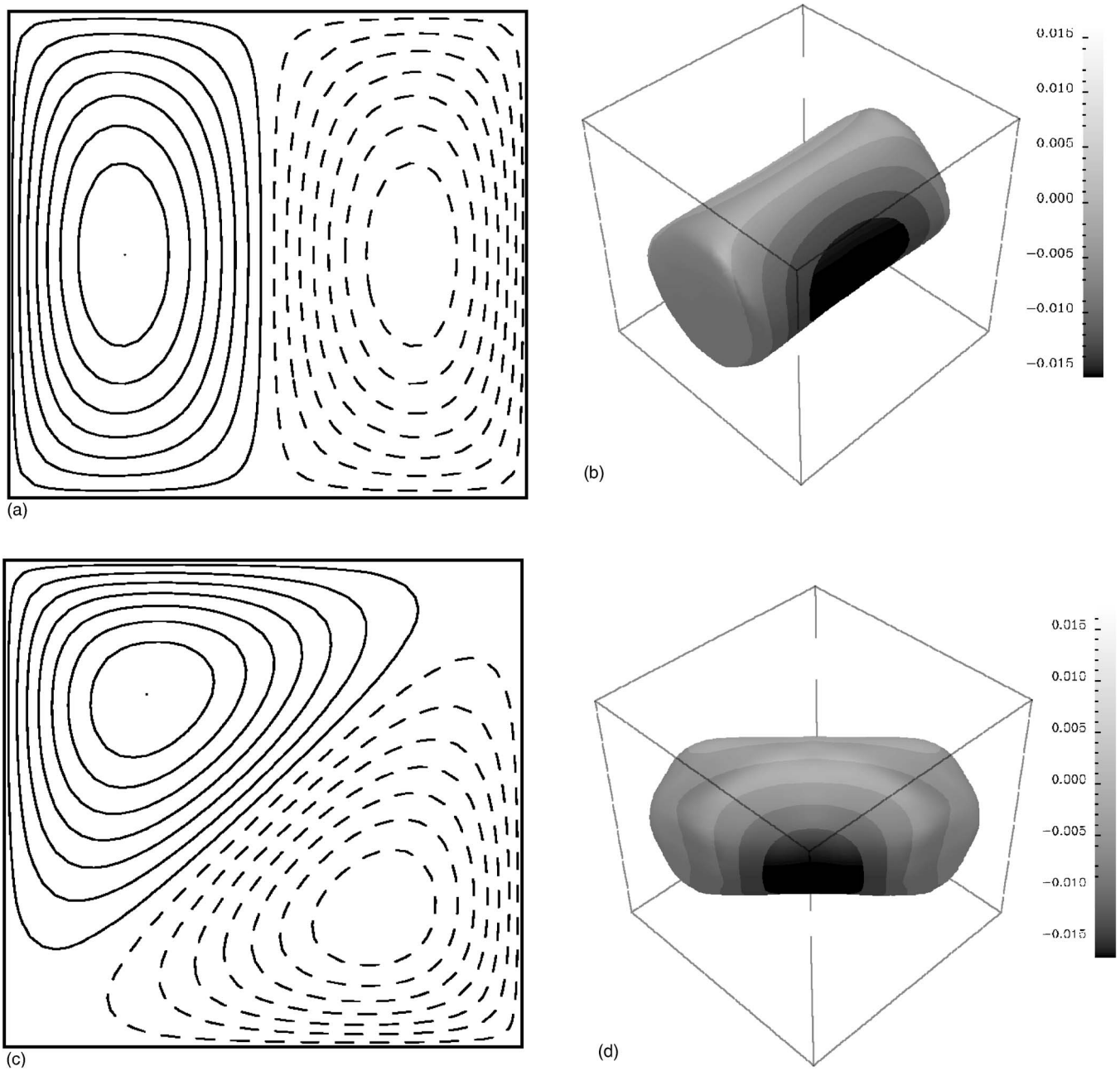

FIG. 5. B_1 and B_2 flow patterns at Ra=3400. Vertical velocity contours at the horizontal midplane $z=0$ for the (a) B_1 and (c) B_2 flow patterns. Positive and negative values of the velocity are plotted with solid and dashed lines, respectively. Surfaces of $\lambda_2=0$ for the (b) B_1 and (d) B_2 flow patterns. The gray levels are scaled with the value of the vertical velocity component.

(unstable) flow patterns become more complex. Figure 7(a) shows that the unstable B_1 solution at $\mathrm{Ra}=1.5\times10^5$ keeps the y roll configuration, but with four pairs of secondary rolls aligned in the x direction. Two of these pairs arise near the top wall, while the other two symmetrical pairs develop near the bottom wall. In addition, two pairs of weak secondary vortical structures, which arise at two diagonally opposing edges of the cavity, are portrayed in Fig. 7(a). Projections of velocity vectors into vertical planes with y constant, not shown here, reveal that whereas these projections are almost circular at Ra=3500, they tend to become rectangular with a slight elongation in the $x=z$ direction at $\mathrm{Ra}=1.5\times10^5$. Figures 7(b) and 8(a) show that the diagonal roll configuration of the stable B_2 solution elongates in the negative diagonal direction $x=-y$ at $\mathrm{Ra}=1.5\times10^5$. Figure 7(b) also reveals that the B_2 flow pattern has developed secondary vortical structures parallel to the horizontal edges of the cavity. The secondary recirculations near the four corners shown in Fig. 8(b) are the projection into the vertical diagonal plane $x=y$ of these secondary vortical structures. The stable B_3 solution depicted in Fig. 7(c) displays vortical structures parallel to the horizontal edges of the cavity which are superimposed onto its characteristic four half connected rolls spatial structure. Finally, Fig. 7(d) shows that the toroidal shape of the unstable B_4 solution, with silicone oil raising near the lateral walls and sinking through the central part of the cavity, is

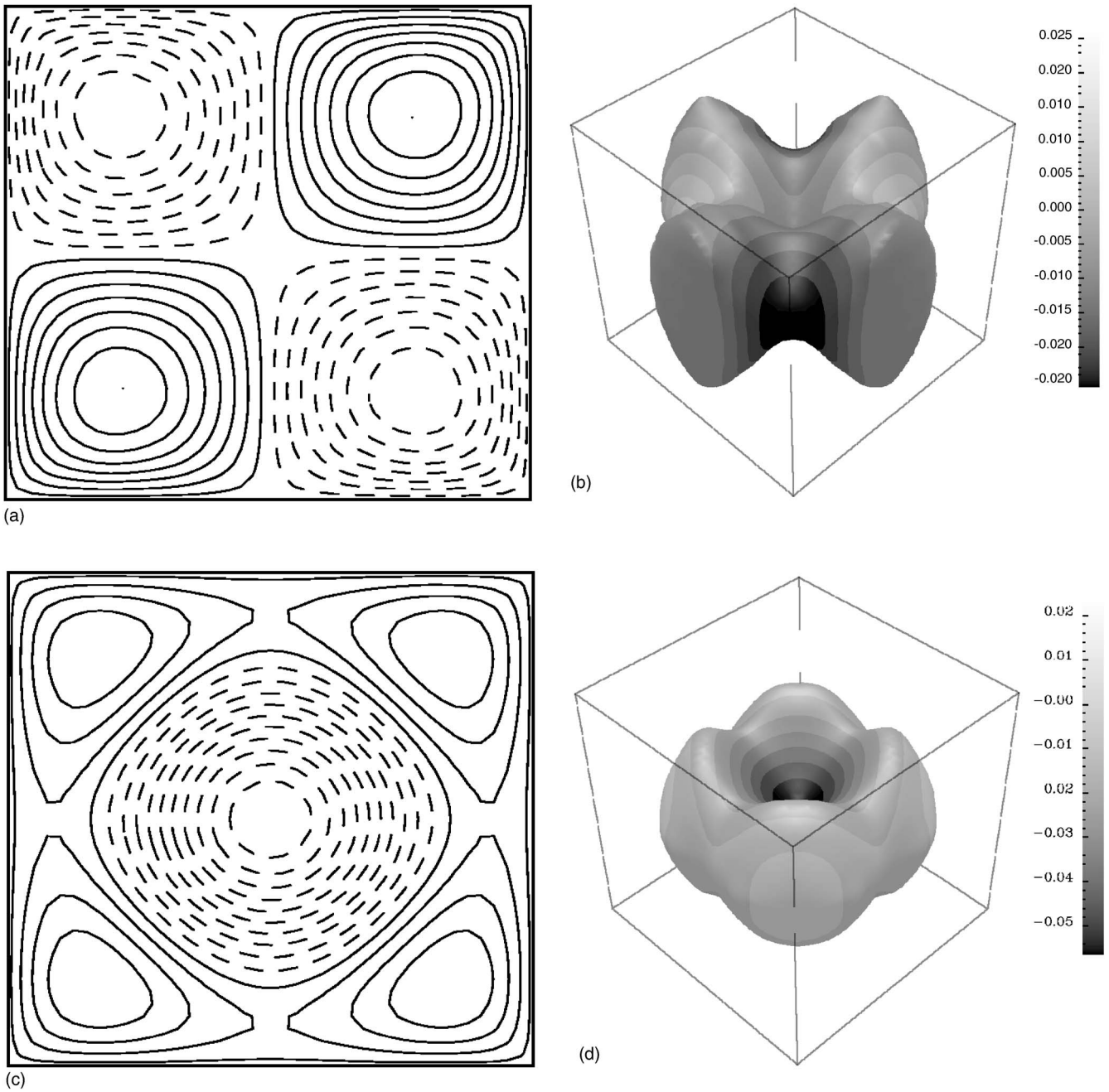

FIG. 6. B_3 and B_4 flow patterns at values of Ra slightly above the bifurcation points where they set in. Vertical velocity contours at the horizontal midplane $z=0$ for the (a) B_3 at Ra=5950 and (c) B_4 at Ra=7600 flow patterns. Positive and negative velocity values are plotted with solid and dashed lines, respectively. Surfaces of $\lambda_2=0$ for the (b) B_3 and (d) B_4 flow patterns. The gray levels are scaled with the value of the vertical velocity component.

only kept near the bottom wall. In the rest of the cavity the flow raising along the central region tends to recirculate towards the four vertical edges before sinking.

3. Secondary bifurcations and flow patterns

Figure 2(b) shows that the stability character of the B_3 flow pattern at Pr=130 is analogous to that reported at Pr =0.71 [19]. At both Prandtl numbers the B_3 solution is unstable when it originates at $\mathrm{Ra}_b=5904$ with a positive double eigenvalue. This double eigenvalue becomes negative, i.e., the B_3 solution becomes stable, at $\mathrm{Ra}_b=9857$ (Pr=130) and $\mathrm{Ra}_b=8278$ (Pr=0.71). Once stable, the B_3 solution remains so for values of Ra up to at least 1.5×10^5 for both Prandtl numbers. Figure 2(b) also shows that two additional unstable flow patterns, denoted as B_{31} and B_{32}, develop at the bifurcation point where the B_3 flow pattern becomes stable. Both solutions have lost two of the symmetries of the B_3 pattern, as indicated in Table III. Flow patterns B_{31}, B_{32} and those that appear at their subsequent bifurcations remain unstable over the whole range of Ra investigated.

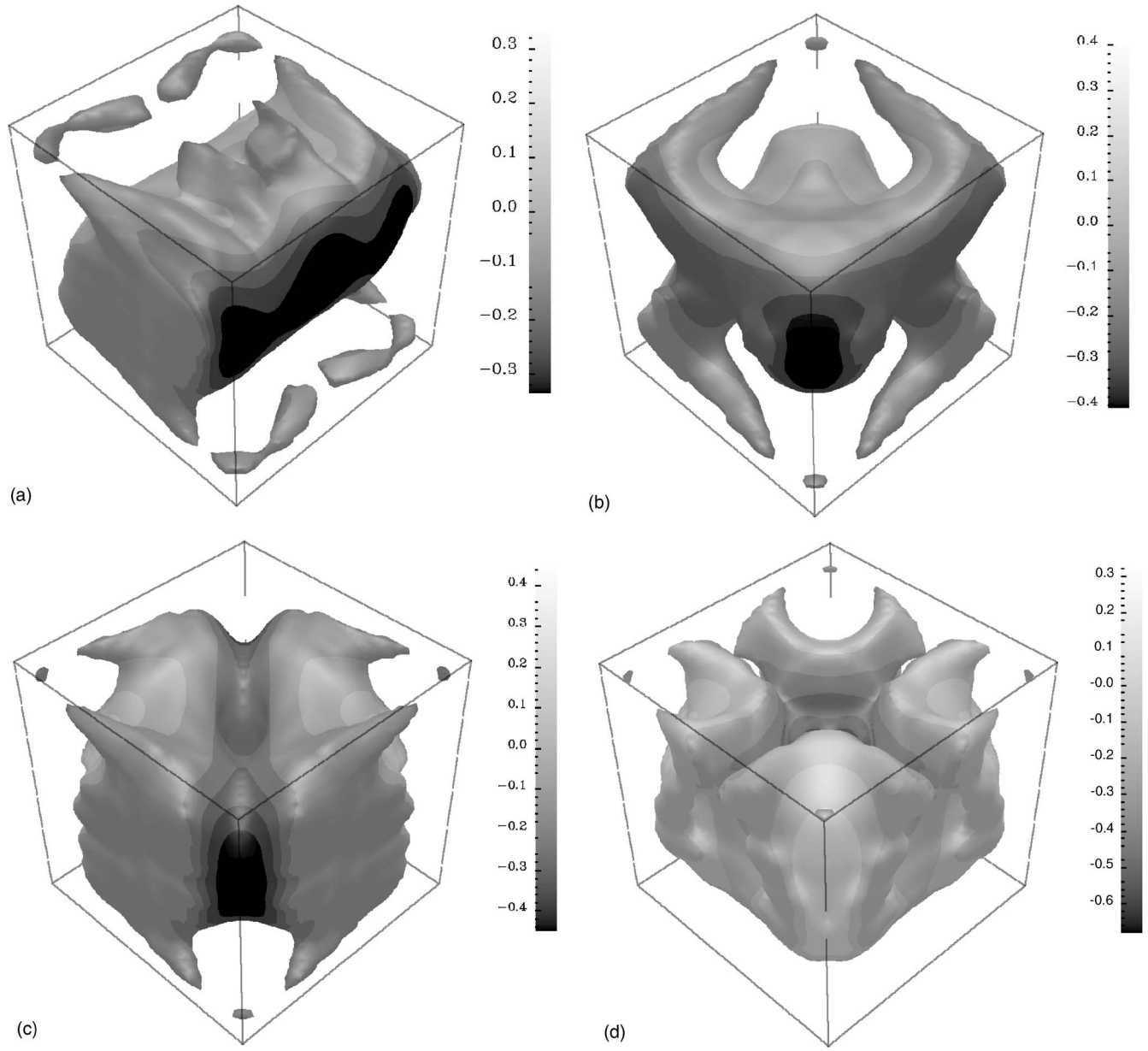

FIG. 7. Surfaces of $\lambda_2=0$ for the (a) B_1, (b) B_2, (c) B_3, and (d) B_4 flow patterns at $\mathrm{Ra}=1.5\times10^5$. The gray (color) levels are scaled with the value of the vertical velocity component.

The B_1 solution is stable when it sets in and remains stable until a symmetry-breaking bifurcation takes place at $\mathrm{Ra}_b=51\,155$, as shown in Fig. 2(a) and Table III. At this bifurcation point the B_1 flow pattern becomes unstable and a new stable flow pattern named B_{11} develops. This bifurcation is analogous to that previously reported for $\mathrm{Pr}=0.71$ at $\mathrm{Ra}_b=66\,200$ [19]. Figure 9(a) shows that the B_{11} flow pattern is the result of the superposition into the main y roll of two relatively strong counterrotating secondary vortices near the top cavity wall. This pair of secondary vortices is better portrayed in Fig. 9(b), where isosurfaces of $\lambda_2=0$ are depicted. Unlike the $\mathrm{Pr}=0.71$ case, the B_{11} flow pattern does not remain stable up to $\mathrm{Ra}=1.5\times10^5$, but it becomes unstable at $\mathrm{Ra}_b=61\,383$ and remains so thereafter. At the symmetry-breaking bifurcation point where the B_{11} flow pattern becomes unstable, an initially stable flow pattern denoted as B_{111} develops. The B_{111} flow pattern becomes unstable as a consequence of a Hopf bifurcation occurring at $\mathrm{Ra}_b=122\,500$.

In contrast to the results reported at $\mathrm{Pr}=0.71$ [19] which predicted that the B_2 flow pattern was unstable over the whole region $\mathrm{Ra}<1.5\times10^5$, present results at $\mathrm{Pr}=130$ predict that the initially unstable B_2 flow pattern becomes stable at $\mathrm{Ra}_b=75\,636$ and remains stable up to at least $\mathrm{Ra}=1.5\times10^5$. Figure 2(a) shows that solutions B_1 and B_2 are connected through solution branches that emanate at their secondary bifurcations. Specifically the B_{11} and the B_{21} solutions are connected through the B_{111} solution. The B_{21} flow pattern, which sets in as an unstable solution when the B_2 flow pattern becomes stable at $\mathrm{Ra}_b=75\,636$, is stable within the range $108\,767\leqslant\mathrm{Ra}\leqslant129\,098$. Hence, as the three flow patterns, B_{11}, B_{21}, and B_{111} involved in this connection are

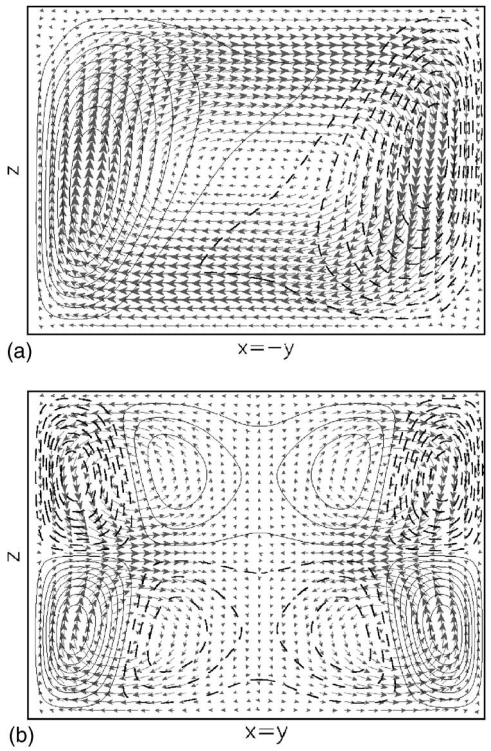

FIG. 8. The diagonal oriented B_2 flow pattern at $\mathrm{Ra}=1.5\times10^5$. Vertical velocity contours and velocity vectors at the vertical diagonal planes $x=-y$ (a) and $x=y$ (b). Positive and negative velocity values are plotted with solid and dashed lines, respectively.

stable for certain ranges of Ra in the region $\mathrm{Ra}\leqslant1.5\times10^5$, it is interesting to analyze the evolution of these flow patterns along the solution branches.

Figures 10(a) and 10(b) show that near the bifurcation point where the B_{111} sets in the flow pattern consists of a main y roll with two superimposed secondary vortices that span the top cavity wall. Therefore, B_{111} has a spatial configuration similar to that of solution B_{11} plotted in Figs. 9(a) and 9(b), except for the loss of the reflection symmetry with respect to the plane $y=0$, denoted as S_y in Table III. Figures 10(c) and 10(d) show that the main roll of B_{111} tends to align diagonally as Ra is increased. These figures also show that the B_{111} flow pattern has no symmetry element. After the turning point at $\mathrm{Ra}_b=140\,028$ the main roll of the B_{111} solution tends to adopt again the characteristic alignment of the y roll flow pattern B_1. Actually, Figs. 10(e) and 10(f) show that back at $\mathrm{Ra}=1.22\times10^5$, near the connection point to the B_{21} solution, the B_{111} flow pattern is mainly an y roll with secondary circulations near the edges of the cavity. These secondary circulations, which are also present in the B_1 solution, are stronger at the two edges in the diagonal direction $y=z$ of the B_{111} flow pattern depicted in Figs. 10(e) and 10(f). On the other hand, near the bifurcation value $\mathrm{Ra}_b=75\,600$ where the B_{21} solution develops, this solution is quite similar to the diagonal-roll flow structure B_2, except for the lost of the diagonal reflection plane. As Ra is increased the main roll of the B_{21} solution tends to align in the y direction. Then, after two turning points that occur at $\mathrm{Ra}_b=141\,840$ and $\mathrm{Ra}_b=120\,150$, the B_{21} and the B_{111} solutions connect through a

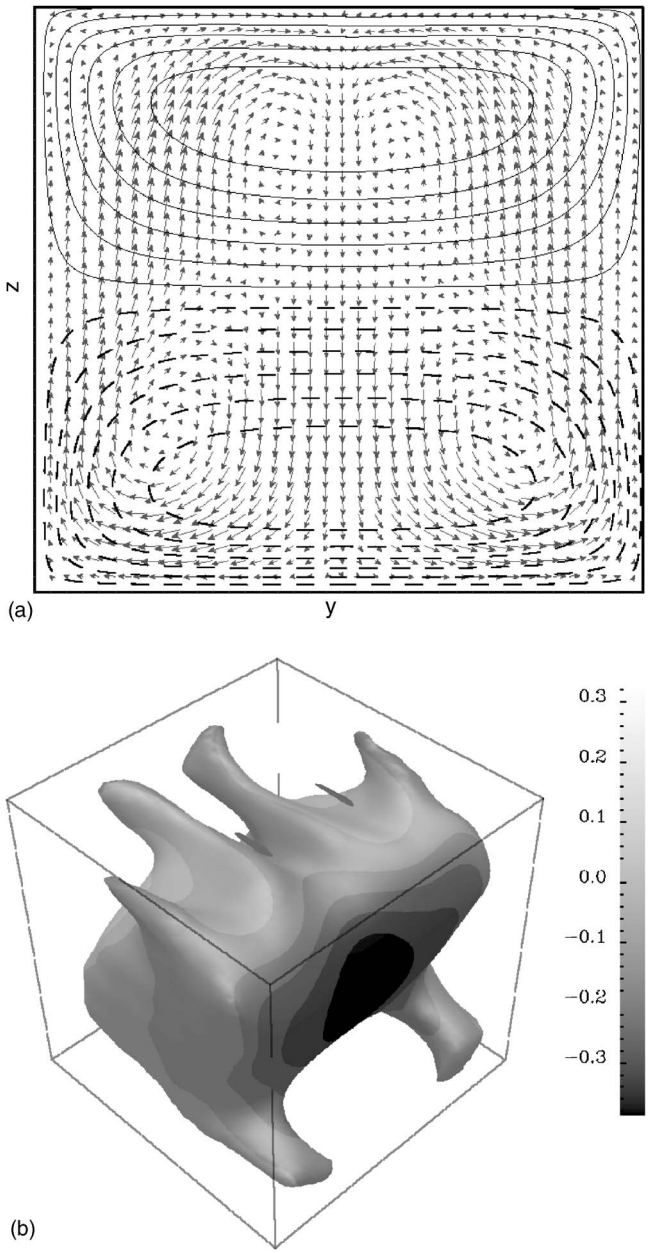

FIG. 9. The B_{11} flow pattern at $\mathrm{Ra}=6\times10^4$. (a) Contours of the velocity component normal to the vertical plane $x=0$, together with the projected velocity vectors. Positive and negative velocity values are plotted with solid and dashed lines, respectively. (b) Surface of $\lambda_2=0$. The gray levels are scaled with the value of the vertical velocity component.

bifurcation point. Near this bifurcation point the B_{21} flow pattern is analogous to that of the B_{111} solution in Figs. 10(e) and 10(f). Further along the solution branch, the B_{21} flow pattern becomes stable at $\mathrm{Ra}_b=129\,098$ and remains stable up to $\mathrm{Ra}_b=108\,767$.

Figure 11(a) depicts the surface $\lambda_2=0$ for the B_{21} flow pattern at $\mathrm{Ra}=1.22\times10^3$ within the region where it is stable. This figure shows that B_{21} has six secondary vortical structures aligned in the x direction. Three of these secondary vortices arise near the top cavity wall, and the other three are the corresponding symmetrical ones which develop near the

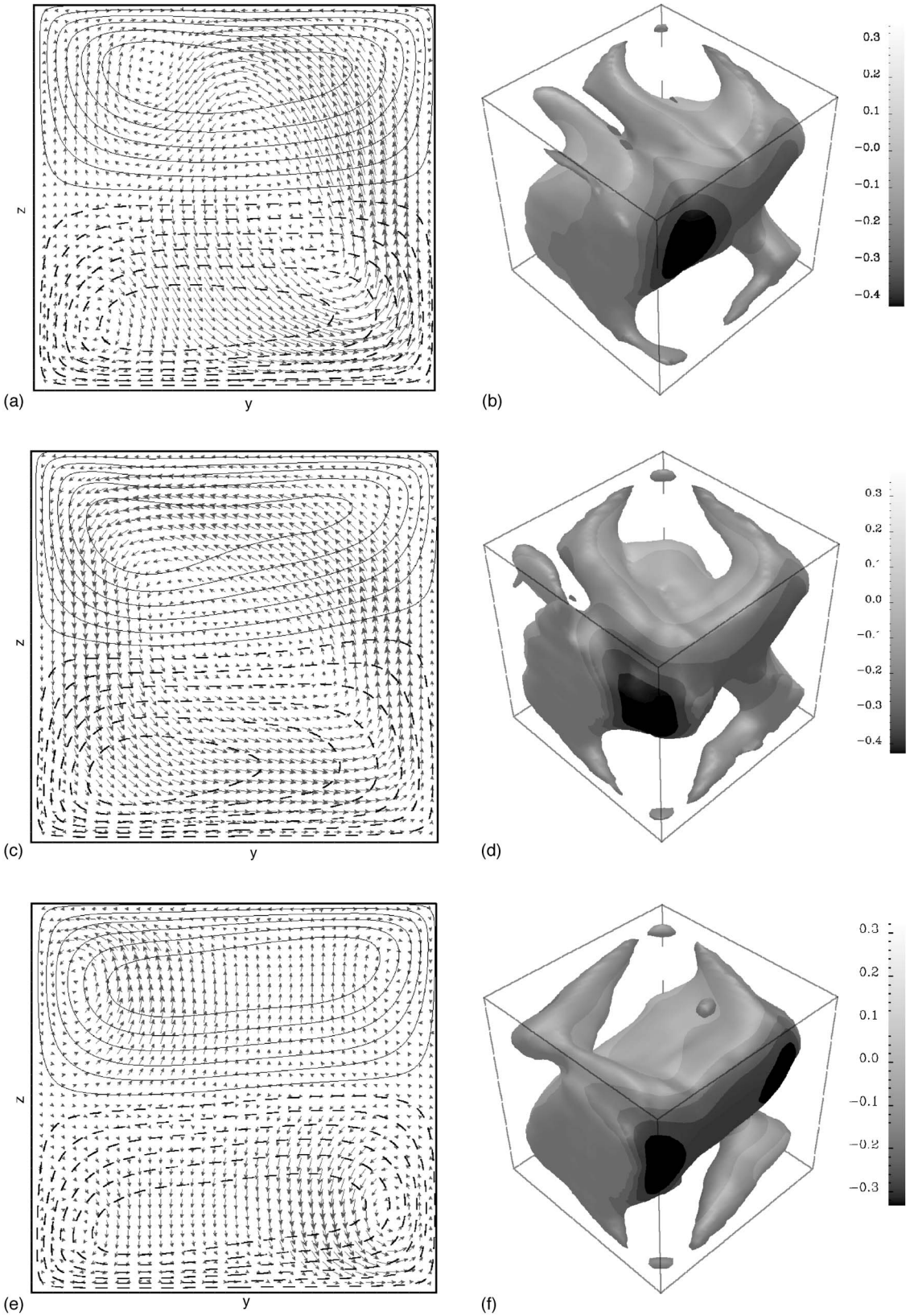

FIG. 10. The B_{111} flow pattern at (a) and (b) $\mathrm{Ra}=7\times10^4$; (c) and (d) $\mathrm{Ra}=1.22\times10^5$; (e) and (f) back at $\mathrm{Ra}=1.22\times10^5$ near the connection with the solution B_{21}. (a), (c), and (e) Contours of the velocity component normal to the vertical plane $x=0$, together with the projected velocity vectors. Positive and negative velocity values are plotted with solid and dashed lines, respectively. (b), (d), and (f) Surfaces of $\lambda_2=0$. The gray levels are scaled with the value of the vertical velocity component.

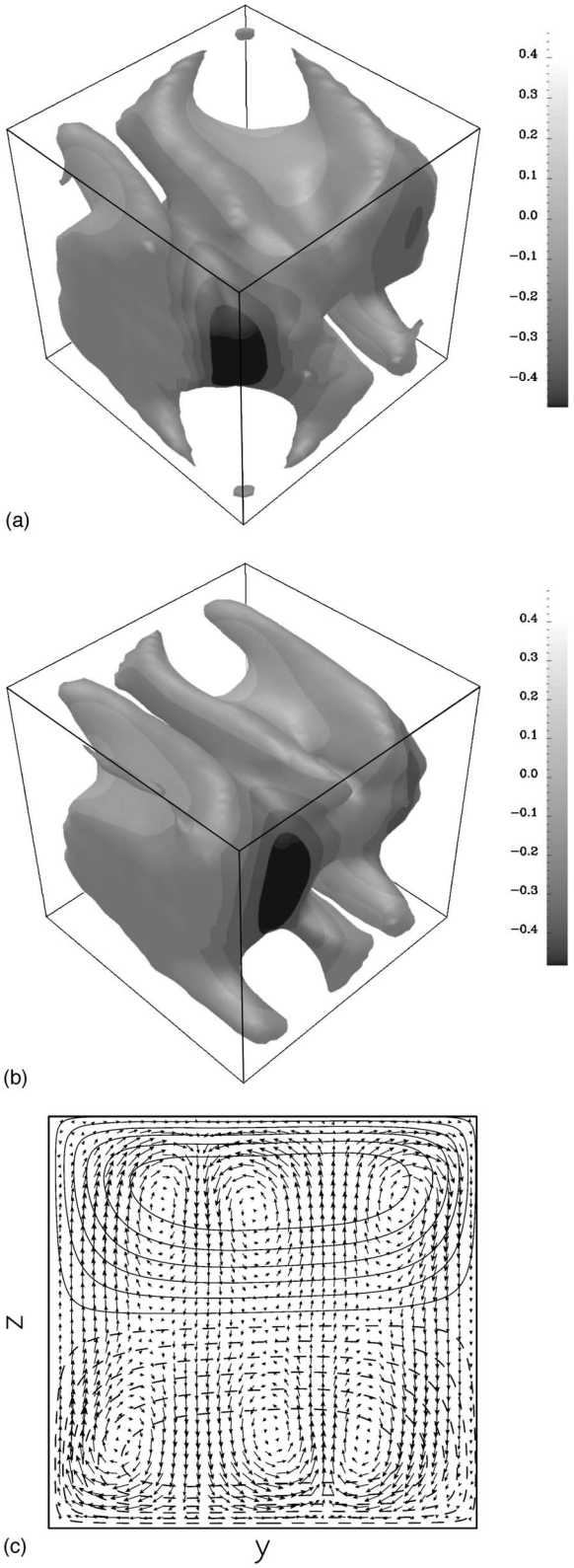

FIG. 11. The B_{21} flow pattern. Surfaces of $\lambda_2=0$ at (a) Ra $=1.2\times10^5$ within the region where it is stable and (b) Ra$=1.5\times10^5$. The gray levels are scaled with the value of the vertical velocity component. (c) Contours of the velocity component normal to the vertical plane $x=0$, together with the projected velocity map at Ra$=1.5\times10^5$. Positive and negative velocity values are plotted with solid and dashed lines, respectively.

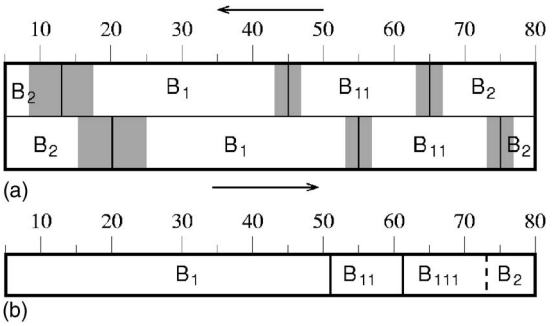

FIG. 12. (a) Sequence of flow transitions from the conductive state observed experimentally by Pallarès *et al.* [20] when the Ra was increased and decreased stepwise (the experimental range of Ra where each transition occurred is indicated by gray strips). (b) Stable flow patterns identified by the current continuation method following the branch of B_1. The dashed line at Ra$=75\,636$ indicates that at this value B_2 becomes stable and therefore both B_{111} and B_2 are stable within the region $75\,636\leqslant \mathrm{Ra}\leqslant 8\times10^4$.

bottom cavity wall. At Ra$=1.5\times10^5$ the main roll of the B_{21} solution has evolved to a y roll and the secondary vortices that span the top and bottom walls align with vorticity perpendicular to that of the main roll, as shown in Figs. 11(b) and 11(c). Thus, present results reveal that the evolution of the B_{21} with Rayleigh number is rather complex. This is clearly reflected by variations in the Nusselt number in the bifurcation diagram. Despite the important change experienced by the B_{21} flow pattern along the solution branch it does not lose the symmetry with respect to the origin represented by $-Id$ in Table III. This is clearly reflected in Figs. 11(b) and 11(c). Note that due to the presence of several turning points in the B_{21} solution branch, three, five or even seven realizations of the flow pattern B_{21} may be possible over certain ranges of Rayleigh number in the region Ra $\leqslant 1.5\times10^5$.

B. Comparison with experiments

Pallarès *et al.* [20] used a particle image velocimetry (PIV) visualization technique to characterize the convective flow patterns in a cubical cavity filled with silicone oil (Pr$=130$). Only steady flow patterns were observed by these authors over the whole range of experimental conditions, $5\times10^3\leqslant \mathrm{Ra}\leqslant 8\times10^4$, except over the initial transitory start-up period of the experiments. These authors measured velocities in two vertical planes and considered that a steady flow pattern was obtained when velocity fields recorded at consecutive times differ only by the experimental error. In the case of adiabatic lateral walls the three stable steady flow patterns reported by Pallarès *et al.* [20] correspond to the current B_1, B_2, and B_{11}. The unstable toroidal flow pattern B_4 was experimentally identified [20] as a transitional state during the startup of the experimental apparatus that eventually evolved to the diagonal roll B_2. This diagonal roll was the the flow structure observed by these authors for $\mathrm{Ra}\leqslant10^4$, as shown in Fig. 12(a). This figure also shows that the diagonal roll B_2 evolved experimentally to the single roll B_1 in the range $10^4<\mathrm{Ra}<3\times10^4$. When Ra was increased from Ra $=5\times10^4$ to Ra$=6\times10^4$ the single roll B_1 evolved to the B_{11}

flow pattern. Beyond $Ra=7\times10^4$ the flow pattern B_{11} was observed by Pallarès *et al.* [20] to evolve to the diagonal roll B_2. Furthermore, these authors [20] reported that a decrease in Rayleigh number reversed the sequence in the pattern formation with a hysteresis effect that shifted transitions to lower values of the Rayleigh number, as illustrated also by Fig. 12(a).

The present study predicts that at the smallest primary bifurcation ($Ra_c=3389$) both the single roll B_1 and the diagonal roll B_2 flow patterns develop. Figures 2 and 3 show that whereas the B_1 flow pattern is stable when it sets in and remains stable until a symmetry-breaking bifurcation takes place at $Ra_b=51\,155$, the B_2 flow pattern sets in as an unstable solution and remains unstable for values of Ra up to $Ra_b=75\,636$. The fact that the initially unstable flow pattern B_2 was found experimentally by Pallarès *et al.* [20] for Rayleigh numbers up to 10^4 is in disagreement with current results. Notwithstanding, the stability analysis for the B_2 solution indicates that the leading eigenvalue has a positive real part which is very close to zero at slightly supercritical Ra values, as shown in Fig. 3. This suggests that any small imperfection of the experimental setup, i.e., any small perturbation of the dynamical system, might have caused this leading eigenvalue to become negative. It is worth noting that the real part of the leading eigenvalue plotted in Fig. 3 is a dimensionless quantity. Taking into account the properties of silicone oil and the dimensions ($12.5\times12.5\times12.5$ mm) of the experimental cavity [20] this dimensionless quantity has to be divided approximately by 1600 to express it in units of s^{-1}. The effect on the flow of a small tilt in the cavity vertical setup has been further investigated by means of an explicit time-marching procedure based on a finite-difference solver [24]. As the computational time needed by a time-marching procedure grows considerably when Pr is increased, time-marching calculations were carried out in a cavity filled with air, i.e., Pr=0.71. A cavity rotated 0.1° around $x=y$ was assumed. The value 0.1° was chosen because it is the maximum deviation in the angle with respect the horizontal plane allowed by the experimental arrangement [20]. First, at Ra=3500, the time marching procedure was initialized with a motionless field and a linear temperature distribution in the z direction. It was found that the flow evolved towards the B_2 flow pattern. Then subsequent time-marching calculation were initialized from a previous convective solution at a different value of Ra. Whereas the B_2 solution was also found when Ra was increased up to $Ra=5\times10^3$, an increment from $Ra=5\times10^3$ to $Ra=10^4$ caused the flow to evolve towards the B_1 flow pattern. However, the transition from B_1 to B_2 occurred within the range $3500\leqslant Ra<5\times10^3$ when the Rayleigh number was decreased. These results suggest that a small tilt in the cavity vertical setup might be sufficient to stabilize the diagonal roll flow pattern B_2, and explaining why this solution was found experimentally at low values of the Rayleigh number.

Figure 12 shows that the symmetry-breaking bifurcation of the B_1 solution leading to the B_{11} solution predicted in the current work is in reasonable agreement with the experimentally observed [20] transition between these two flow structures. Figures 2 and 12(b) show that this solution B_{11} is only stable up to Ra=61 383 where a new symmetry-breaking bifurcation occurs yielding the initially stable B_{111} flow pattern. The B_{111} solution becomes unstable as a consequence of a Hopf bifurcation at $Ra_b=122\,500$. The fact that this transition between B_{11} and B_{111} was not experimentally observed [20] may be due to the difficulty in differentiating between both spatial configuration for values of Ra near the symmetry-breaking bifurcation point, as shown in Figs. 9, 10(a), and 10(b). The experimental range of stability of B_2 ($73\times10^3\leqslant Ra\leqslant8\times10^4$) reported by Pallarès *et al.* [20] is consistent with current results, which predict this stabilization at $Ra_b=75\,636$.

The other numerically predicted stable flow pattern B_3 was not experimentally observed because the basin of attraction of B_3 does not overlap with the initial conditions used in the experiment, which follow the branch of the primary bifurcation yielding the B_1 solution [see Fig. 2(a)].

C. Effect of the Prandtl number

Comparison of the current bifurcation diagram at Pr=130, presented in Fig. 2, with the one previously reported at Pr=0.71 [19], suggests that the evolution of the flow patterns and their subsequent bifurcations with Ra depend on the Prandtl number. Accordingly, the B_1, B_2, B_3, and B_4 flow patterns at $Ra=1.5\times10^5$ and Pr=130, depicted in Fig. 7, are considerably different from the corresponding ones shown in Fig. 13 for Pr=0.71. A comparison between these two plots reveals differences in the shape of the main convection cells as well as in the number and location of secondary rolls. The most striking difference is observed for the B_3 patterns depicted in Figs. 7(c) and 13(c). The typical four half connected rolls structure observed in Fig. 6(b) for the B_3 pattern at Ra=5950 is basically preserved in Fig. 7(c) at $Ra=1.5\times10^5$ for Pr=130. Although the four half connected rolls configuration of B_3 is kept over a wide range of Ra for Pr=130 it is hardly recognizable in Fig. 13(c) for Pr=0.71.

Since differences in the spatial configuration of flow patterns should have an effect on the Nusselt number, the variation of Nu with Pr was analyzed. Figure 14 depicts the variation of Nusselt number with Pr over the range $0.71\leqslant Pr\leqslant130$ for the flow patterns B_1, B_2, and B_3 at six values of Ra. Significant changes of the predicted values of Nu with Pr are observed in the region $0.71\leqslant Pr\leqslant10$ for the three flow patterns and all values of Ra investigated. Variations in Nu are clearly strongest for the B_3 pattern in Fig. 14(c) and much weaker for the B_1 flow pattern in Fig. 14(a). Also, the predicted variation of Nu with Pr tend to be, for any given flow pattern, more pronounced at higher Ra.

It is remarkable that Nu increases slightly with Pr in the region $0.71\leqslant Pr\leqslant10$ for the B_1 flow pattern while it decreases for B_2 and B_3. This different behavior may be related to the distinct action of secondary motions. Flow patterns in Figs. 13(b) and 13(c), corresponding to B_2 and B_3 at $Ra=1.5\times10^5$ and Pr=0.71, display motions near the edges and corners of the cavity that are stronger than those for Pr=130 in Figs. 7(b) and 7(c). The opposite argument is valid for the case of B_1. The flow pattern in Fig. 7(a) at Pr=130 shows two small secondary rolls on top of the main cell which are not present in Fig. 13(a) for Pr=0.71. Thus, the

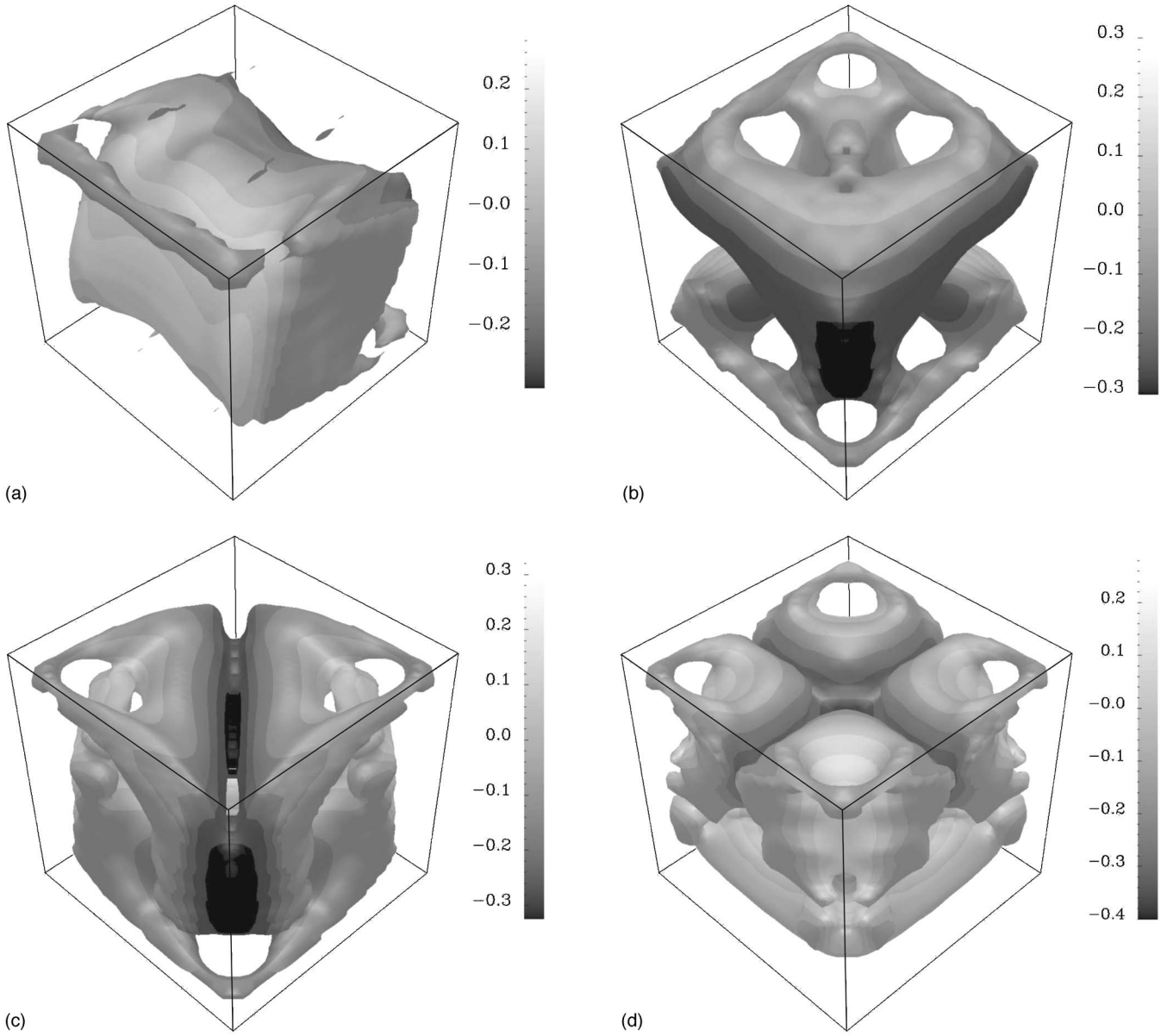

FIG. 13. Surfaces of $\lambda_2=0$ for the flow patterns (a) B_1, (b) B_2, (c) B_3, and (d) B_4 at $\mathrm{Ra}=1.5\times10^5$ and $\mathrm{Pr}=0.71$. The gray levels are scaled with the value of the vertical velocity component.

relative increase or decrease of Nu with Pr may depend on the particular way in which each flow pattern, whose motion becomes progressively stronger as Ra is increased, adapts to the constraints imposed by the bounding walls.

The Nusselt number changes weakly with increasing Pr for $\mathrm{Pr}\geqslant30$, tending to an asymptotic value in the limit $\mathrm{Pr}\rightarrow\infty$. The asymptotic value, marked with an arrow in Fig. 14, corresponds to the Nusselt number obtained when Pr^{-1} is replaced by zero in the governing equations (1) and (2), which is equivalent to consider $\mathrm{Pr}=\infty$. From a mathematical point of view this asymptotic behavior can be explained by the fact that the inverse of the Prandtl number is a factor that multiplies the nonlinear terms in Eq. (1). Hence, an increase in Prandtl number decreases the effects of the nonlinear terms, which for a fixed value of Ra can be seen as perturbation effects in Eq. (1). It is also worth mentioning that the theoretical model recently proposed by Grossmann and Lohse [13,26] for the scaling of Rayleigh-Bénard convection postulates the existence of a very large Prandtl number regime where Nu is independent of Pr.

IV. CONCLUSIONS

A continuation procedure based on a Galerkin spectral method has been used to determine the bifurcation diagram of steady flow patterns inside a cubical cavity heated from below for values of the Rayleigh number up to 1.5×10^5. The cavity is filled with silicone oil ($\mathrm{Pr}=130$) and the four lateral walls are assumed to be adiabatic. Fifteen solution branches have been tracked and visualized in terms of the variation of Nusselt number with Ra. The stability analysis predicts that six steady flow patterns (B_1, B_{11}, B_{111}, B_2, B_{21}, and B_3) are stable over certain ranges of Ra in the region $\mathrm{Ra}\leqslant1.5\times10^5$. Present results reveal the importance of taking into

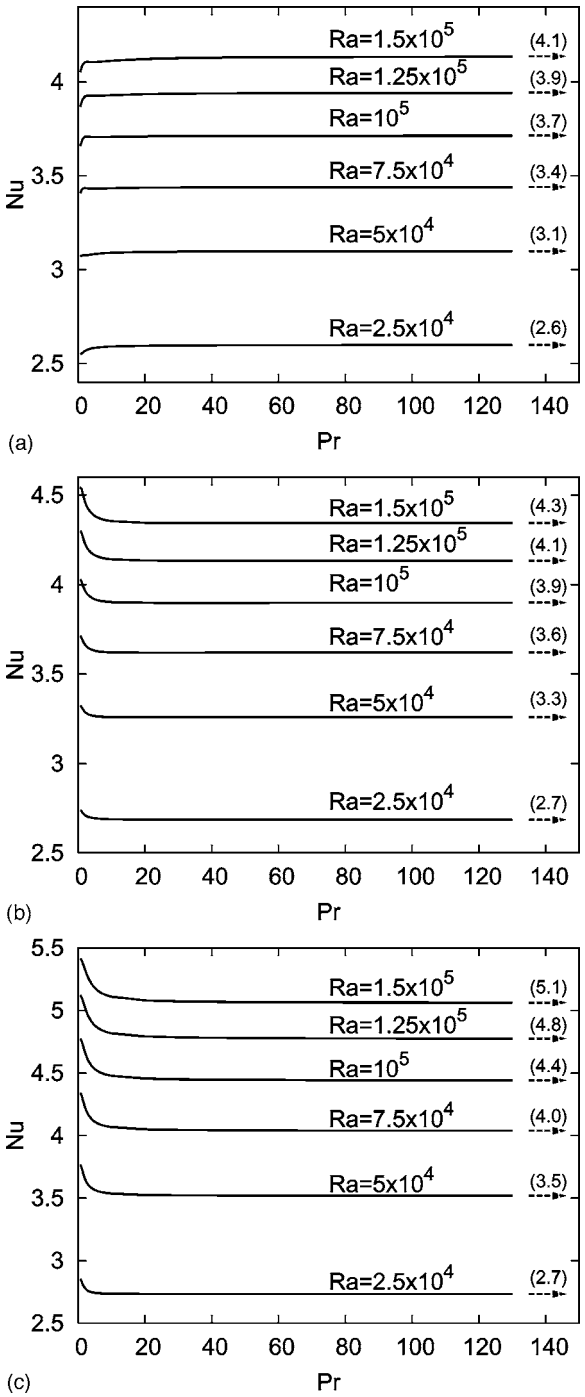

FIG. 14. Variation of the Nusselt number as a function of the Prandtl number for the flow patterns (a) B_1, (b) B_2, and (c) B_3. The values inside parenthesis above the arrows correspond to asymptotic Nusselt values for $\mathrm{Pr}=\infty$.

account unstable convective flow patterns because they can become stable as a consequence of subsequent bifurcations.

On the other hand, several Hopf bifurcations have been identified within the region $\mathrm{Ra} \geqslant 9 \times 10^4$. In particular, the B_{111} flow pattern loses its stability through a Hopf bifurcation at approximately $\mathrm{Ra}=122\,500$. This suggests that time-dependent flow patterns are likely to occur beyond $\mathrm{Ra}=10^5$. Future research will be oriented to further develop the present method in order to investigate both steady and time-dependent flow patterns over a wider range of Rayleigh numbers.

The symmetry properties of flow patterns have been useful for analyzing their spatial configuration. Some of the flow patterns identified in the present work evolve to rather complex spatial configurations as the Rayleigh number increases. In general, all flow patterns tend to develop secondary rolls as the Rayleigh number increases. Note that in a recent work reported by Sun *et al.* [16] on turbulent Rayleigh-Bénard convection in a cylindrical cell of aspect ratio one secondary rolls were observed experimentally. It has been checked that an important change in the spatial configuration of a flow pattern along a solution branch is clearly reflected as a significant change in the corresponding heat transfer at the bottom and top cavity walls.

Present results are in reasonable agreement with the experimental results reported by Pallarès *et al.* [20]. Most of the experimental flow transitions between different steady flow patterns observed by these authors over the region $\mathrm{Ra} \leqslant 8 \times 10^4$ are explained by current results.

Bifurcation diagrams depend strongly on the Prandtl number and the evolution of flow patterns as the Rayleigh number increases is also rather dependent on Pr. The variation of the Nusselt number Nu with Pr reveals that heat transfer rates for any of the three stable solutions that set in at bifurcations from the conductive state change significantly within the region $0.71 \leqslant \mathrm{Pr} \leqslant 10$, tending to an asymptotic value beyond.

ACKNOWLEDGMENTS

The authors D.P., J.H., and F.G. are grateful for the financial support received from DGICYT project FIS2005-07194 and from the CIRIT "Programa de Grups de Recerca Consolidats de la Generalitat de Catalunya," project 2005SGR-00735. F.G. acknowledges the support received from the *Distinció a la Recerca de la Generalitat de Catalunya*. C.S. has been supported by Grants DGICYT BFM2003-09504-C02-01 (Spain) and CIRIT 2001 2005SGR—01028 (Catalonia).

[1] E. L. Koschmieder, *Bénard Cells and Taylor Vortices* (Cambridge University Press, Cambridge, 1993).

[2] A. V. Getling, *Rayleigh-Bénard Convection: Structures and Dynamics*, Vol. 11 of *Advanced Series in Nonlinear Dynamics* (World Scientific Publishing, Singapore, 1998).

[3] E. Bodenschatz, W. Pesch, and G. Ahlers, Annu. Rev. Fluid Mech. **32**, 709 (2000).

[4] S. Chandrasekhar, *Hydrodynamic and Hydromagnetic Stability* (Clarendon Press, Oxford, 1961).

[5] S. H. Davis, J. Fluid Mech. **30**, 465 (1967).

[6] I. Catton, Int. J. Heat Mass Transfer **15**, 665 (1972).
[7] J. Buell and I. Catton, ASME J. Heat Transfer **105**, 255 (1983).
[8] A. Y. Gelfgat, J. Comput. Phys. **156**, 300 (1999).
[9] J. Mizushima and T. Nakamura, J. Phys. Soc. Jpn. **72**, 197 (2003).
[10] J. P. Gollub and S. V. Benson, J. Fluid Mech. **100**, 449 (1980).
[11] B. Castaing, G. Gunaratne, F. Heslot, L. Kadanoff, A. Libchaber, S. Thomae, X.-Z. Wu, S. Zaleski, and G. Zanetti, J. Fluid Mech. **204**, 1 (1989).
[12] R. M. Kerr and J. R. Herring, J. Fluid Mech. **419**, 325 (2000).
[13] S. Grossmann and D. Lohse, Phys. Rev. Lett. **86**, 3316 (2001).
[14] J. J. Niemela and K. R. Shreenivasan, J. Fluid Mech. **481**, 355 (2003).
[15] R. Verzicco and R. Camussi, J. Fluid Mech. **477**, 19 (2003).
[16] C. Sun, K.-Q. Xia, and P. Tong, Phys. Rev. E **72**, 026302 (2005).
[17] E. Brown, A. Nikolaenko, and G. Ahlers, Phys. Rev. Lett. **95**, 084503 (2005).
[18] I. Catton, Transactions of the ASME, pp. 186–188 (1970).
[19] D. Puigjaner, J. Herrero, F. Giralt, and C. Simó, Phys. Fluids **16**, 3639 (2004).
[20] J. Pallarès, M. Arroyo, F. X. Grau, and F. Giralt, Exp. Fluids **31**, 208 (2001).
[21] L. Harris and W. H. Reid, ASME J. Heat Transfer **93**, 188 (1959).
[22] R. B. Morgan, Math. Comput. **65**, 1213 (1996).
[23] D. Puigjaner, Ph.D. thesis, Facultat de Matemàtiques, Universitat de Barcelona, Barcelona, Spain (2005).
[24] Y. D. Spasov, J. Herrero, F. X. Grau, and F. Giralt, Phys. Fluids **15**, 134 (2003).
[25] J. Jeong and F. Hussain, J. Fluid Mech. **285**, 69 (1995).
[26] S. Grossmann and D. Lohse, Phys. Rev. E **66**, 016305 (2002).